The Role of Optical Phonon Confinement in the Infrared Dielectric Response of III-V Superlattices

Joseph R. Matson,[1] Md Nazmul Alam,[2] Georgios Varnavides,[3] Patrick Sohr,[2] Sean Knight,[5-7] Vanya Darakchieva,[5-7] Megan Stokey,[4] Mathias Schubert,[4,5] Ayman Said,[8] Thomas Beechem,[9] Prineha Narang,[10] Stephanie Law,[2,11] Joshua D. Caldwell[*1,12]

1. Interdisciplinary Materials Science Program, Vanderbilt University, Nashville, TN 37212, USA.
2. Department of Materials Science and Engineering, University of Delaware, Newark DE 19716 USA
3. John A. Paulson School of Engineering and Applied Sciences, Harvard University, Cambridge, MA 02138, USA
4. Department of Electrical and Computer Engineering, University of Nebraska-Lincoln, Lincoln, NE 68588, USA
5. Solid State Physics and NanoLund, Lund University, 22100 Lund, Sweden
6. Competence Center for III-Nitride Technology, C3NiT - Janzèn , Linköping University, 58183 Linköping, Sweden
7. Terahertz Materials Analysis Center (THeMAC), Linköping University, 58183 Linköping, Sweden
8. Advanced Photon Source, Argonne National Laboratory, Argonne, Illinois 60439, USA
9. School of Mechanical Engineering and Birck Nanotechnology Center, Purdue University, West Lafayette, IN, 47907, USA
10. Physical Sciences Division, College of Letters and Science, University of California, Los Angeles (UCLA), CA, USA
11. Department of Materials Science and Engineering, Pennsylvania State University, University Park, PA 16802, USA
12. Department of Mechanical Engineering, Vanderbilt University, Nashville, TN 37212, USA
**Corresponding Author*

Keywords: Phonons, Infrared, Confinement, Spectroscopy

Abstract:

Polar dielectrics are key materials of interest for infrared (IR) nanophotonic applications due to their ability to host phonon-polaritons (PhPs) that allow for low-loss, subdiffractional control of light. The properties of phonon-polaritons are limited by the characteristics of optical phonons, which are nominally fixed for most “bulk” materials. Superlattices composed of alternating atomically-thin materials offer control over crystal anisotropy through changes in composition, optical phonon confinement, and the emergence of new modes. In particular, the modified optical phonons in superlattices offer the potential for so-called crystalline hybrids whose IR properties cannot be described as a simple mixture of the bulk constituents. To date, however, studies have primarily focused on identifying the presence of new or modified optical phonon modes rather than assessing their impact on the IR response. This study focuses on assessing the impact of confined optical phonon modes on the hybrid IR dielectric function in superlattices of GaSb and AlSb. Using a combination of first principles theory, Raman, FTIR, and spectroscopic ellipsometry, the hybrid dielectric function is found to track with the confinement of optical phonons, leading to optical

phonon spectral shifts of up to 20 cm^{-1}. These results provide an alternative pathway towards designer IR optical materials.

Intro:

Phonons play a key role in dictating many material properties, including acoustic, thermal, electronic, and optical properties. Optical phonons within polar crystals offer a principal driver for nanophotonics in the mid- to far-IR[1–3], as they enable the excitation of phonon polaritons (PhPs) that offer lower losses and higher quality factors compared to plasmon counterparts.[4,5] However, PhPs suffer from limited spectral tunability as they can only be supported within the relatively narrow, nominally fixed spectral window bound by the transverse (TO) and longitudinal optical (LO) phonons of the host crystal[6]. Therefore, there is significant interest in exploring methods for tuning the optical phonon response, such as through alloying[7,8], ion intercalation[9], or manipulating the isotopic content[10–12], carrier concentration[13,14], or strain[15–20] in the material.

Beyond these extrinsic factors, phonons can also be modified intrinsically by changing the periodicity of the solid. This has been demonstrated by several recent studies that have leveraged crystalline anisotropy to control PhPs. In hBN[21,22] it was shown that the crystal anisotropy results in optical phonons with different energies along in and out-of-plane crystal axes, causing the PhPs to become hyperbolic due to the opposite sign of the real part of the permittivity tensors along these directions at a given spectral frequency[23]. These hyperbolic phonon polaritons (HPhPs) are of great interest due to their volume confinement[22,24], frequency-dependent propagation[25], and large wavevectors[26]. MoO_3, with its orthorhombic crystal structure giving rise to permittivity tensors that are different along all three axes has given rise to a platform for hosting in-plane HPhPs,[27,28] which propagate at fixed directions in-plane as well as through the volume within specific frequency ranges, providing enormous utility for steering light propagation in planar optical applications[29–33]. More recently, monoclinic crystals have even been shown to host exotic polaritonic behaviors where both the polariton wavevector and the propagation direction disperse as a function of frequency via hyperbolic shear polaritons[34], demonstrating the strong tie between crystal structure and nanophotonic behavior.

While natural crystals offer a broad toolbox of optical phonons, the lack of control over bulk phonon properties remains challenging. Instead, manipulating the crystal structure at an atomic-scale offers a new degree of phonon control. Twisted two-dimensional slabs (i.e., “twist-optics”), for example, can modify the hyperbolicity of PhPs[30–32,35,36] and serve as a method towards achieving active tuning[37]. Alternatively, so-called crystalline hybrids can be created via more traditional semiconductor superlattices (periodic stacks of thin films) to sculpt the IR response[38,39]. Ratchford et al.[38] demonstrated that the confined and interface phonon modes that occur in atomic-scale superlattices of GaN and AlN are capable of significantly altering the IR dielectric function. The resulting material, with its new hybrid dielectric function, enables a suite of extremely dispersive elliptical and hyperbolic polaritons as a result of the complex phonon interactions and superlattice anisotropy. However, due to the large lattice mismatch between GaN and AlN, isolation of the role of the superlattice periodicity from that of strain is non-trivial. Thus, while the initial crystalline hybrid work demonstrated the power of using superlattice modifications to dictate the optical phonons to create new IR nanophotonic materials, in order to predictively design such systems using this approach, it is necessary to develop our understanding of the emergent phonon behavior and determine how this impacts the IR optical properties (i.e., the dielectric function) of the resultant hybrid material.

In semiconductor superlattices, phonons behave differently from those in bulk constituent materials. Acoustic phonons in differing superlattice layers have largely overlapping energy ranges and long wavelengths due to the nature of their dispersion. They are thus able to propagate through the entire superlattice, undergoing zone-folding due to the long-range periodicity within the structure[40,41]. These folded phonons can be used to modify the thermal conductivity of the structure as a function of the superlattice periodicity[42,43] . In SiC this behavior is observed for optical phonons as well, with this zone-folding resulting from the different super-cell lattice stacking within the multiple natural polytypes[44], which can interact with transverse phonon polaritons[45], potentially offering a route towards electrically pumped mid-infrared emitters. However, for superlattices where the optical phonons in different layers occur at different energies, the optical phonons can become confined within a single material layer, resulting in a so-called confined phonon[46–51]. In addition, new phonons resulting from the modified bonding, strain and local dielectric environments occurring at the interfaces between superlattice layers are also observed[52]. The combination of these modifications to the optical phonon properties is the basis for the anticipated modifications in the IR dielectric functions at the heart of the crystalline hybrid approach.

Optical phonon confinement has been extensively demonstrated in Raman scattering studies for superlattices in multiple material systems[38,46,49,53,54] and has even been observed in a singular thin film[55]. The confinement of the optical phonon manifests in Raman measurements as a spectral shifting of the optical phonon frequencies as well as the introduction of additional TO and LO phonons. These confined phonons have been described as sampling the bulk phonon dispersion along the confinement direction, with the momentum given by:

$$\mathrm{k(m)} = \frac{2\pi \mathrm{m}}{(\mathrm{n}+\delta)\mathrm{d}_0}, \quad \mathrm{m} = 1,2,\ldots,\mathrm{n} \tag{1}$$

where m is the mode order, n is the number of monolayers (ML) in the confined layer, d_0 is the lattice constant, and δ is a correction term that is typically attributed to the interface leakage – i.e. how many MLs past the interface are included in the phonon oscillation[50,51]. The δ term has typically been assumed to be 0 or 1, indicating that the atomic displacement from the phonon stops at the interface or the first atom (half of a ML on both sides) past the interface.

Most studies of confined phonons have relied on superlattices with layer thicknesses on the order of tens of MLs, supporting many higher-order modes. This approach is an efficient way to probe the phonon confinement using Raman spectroscopy investigations and has been considered as an alternative to neutron scattering measurements for mapping the optical phonon dispersion. However, using superlattices with large layer thicknesses results in weakly shifted first-order modes and small deviations between the higher-order confined phonons. On the other hand, while confined phonons have been observed in individual thin-films[55], establishing general relevance in applications of nanoscale materials, the limited optical interaction with a single confined layer precludes thorough investigation with most spectroscopic techniques. Instead, to explore the tunability of the principle ($m = 1$) confined mode, which we expect to be the primary driver for the IR optical response, we vary individual atomic-scale layer thicknesses, with monolayer precision, across a number of superlattices – while relying on high numbers of superlattice periods to provide the necessary optical response for thorough characterization.

Our initial investigations into the effect of phonon confinement on the off-Γ phonon dispersion were undertaken through high-energy-resolution inelastic x-ray scattering and *ab-initio* superlattice phonon

dispersion calculations. Our results suggest that phonon confinement presents a controlled way to significantly tune the optical phonon properties for potential applications in IR optics, as well as potential applications in modifying optical phonon scattering.

Main

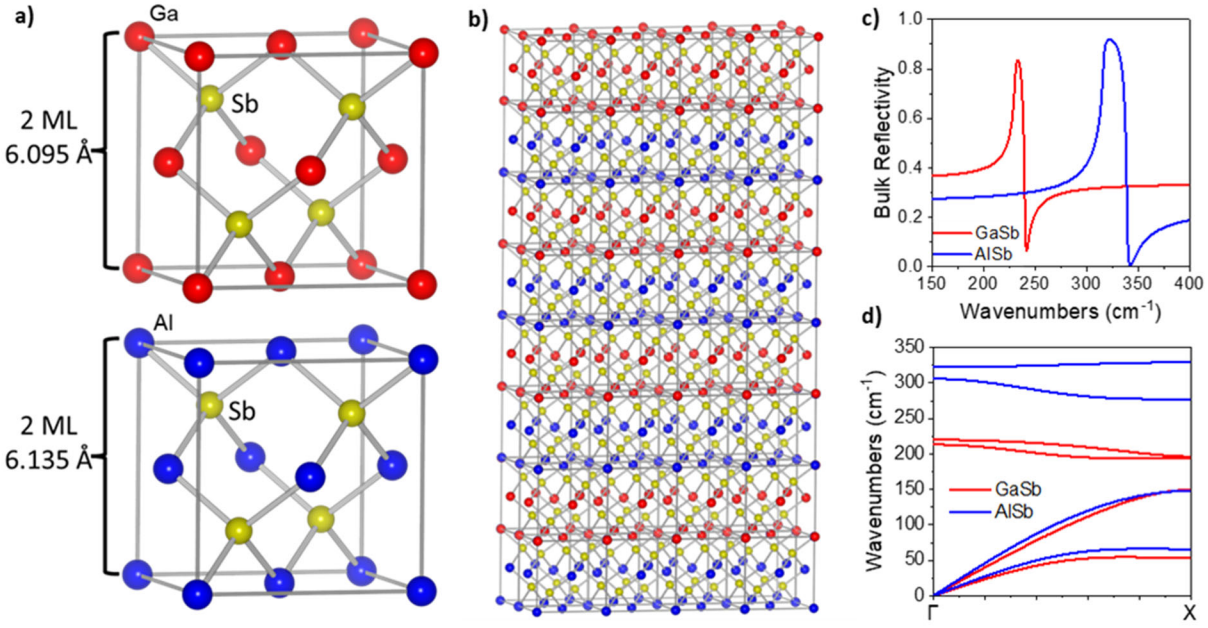

Figure 1: Superlattice Diagram. a) Zincblende unit cells of GaSb (red), and AlSb (blue). b) Diagram of 2ML/2ML superlattice. c) Bulk Reflectivity of constituent materials. d) Phonon dispersion plots of bulk GaSb (red) and AlSb (blue) along the Γ-X Brillouin zone (superlattice direction). Crystal structure visualization produced with VESTA[56].

The initial proof-of-concept demonstration of crystalline hybrid materials showed the ability to create a modified dielectric material with novel nanophotonic properties through deterministic, atomic-scale superlattice design. However, while the AlN/GaN superlattices studied previously[38,57] host polaritons within a technologically important atmospheric window, the large lattice mismatch and partial overlap of the Reststrahlen bands in GaN and AlN leads to strain-induced phonon shifts in addition to a suite of new confined, quasi-confined, and unconfined phonons that limit predictive design. To isolate and explore the impact of optical phonon confinement upon the IR dielectric function, here we leverage superlattices of GaSb and AlSb (Fig. 1a,b). This system offers a two materials with a very small lattice mismatch to minimize strain, while exhibiting two spectrally separate Reststrahlen bands (Fig. 1 c,d), and a shared cation (Sb) to minimize the interface phonon contribution. Thin films of GaSb and AlSb are currently used in optoelectronic devices such as IR detectors and lasers[58–60], so high-quality growth is also well developed. In addition, the zinc blende structure (Fig. 1a) makes the bulk constituent materials optically isotropic, simplifying measurements and dielectric function modeling. The superlattices employed here were grown using molecular beam epitaxy (MBE), enabling ML-level control of layer thickness and high-quality interfaces[61].

While this system allows us to minimize the role of strain-induced phonon shifts, we cannot completely eliminate these effects as there is still a small lattice mismatch between AlSb and GaSb. Though thorough studies have not been done on such large-scale GaSb/AlSb superlattices, we make some initial

approximations on the scale of strain shifts within our superlattice (see supplemental) and note that it is expected to be on the order of 0.5-1% of the phonon frequency. Hence the strain cannot account for the majority of the observed spectral shifts, and thus, those effects derived from phonon confinement.

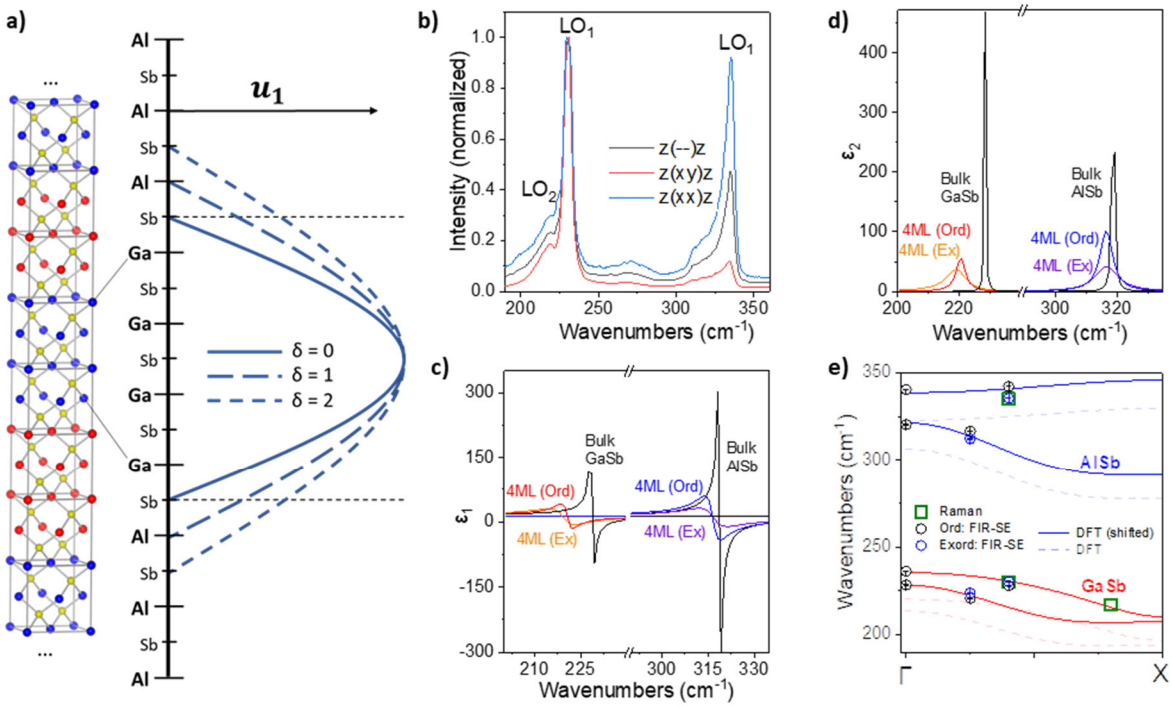

Figure 2: Phonon confinement in 4 ML GaSb /4 ML AlSb superlattice. a) schematic of 4 ML/4ML superlattice, with atomic displacement ***u*** *shown for* m=1 *mode along the superlattice direction. Dashed lines indicate different δ values are shown, to illustrate the impact of the interface leakage term. b) Unpolarized and polarization-resolved Raman spectra of 4ML/4ML superlattice, with single LO phonon (LO_1) observed in the AlSb range, and 2 LO phonon peaks observed in the GaSb range (LO_1, LO_2). c-d) Real (c) and imaginary (d) permittivity for the 4ML GaSb and AlSb layers, in the ordinary and extraordinary axes, compared to the bulk dielectric functions (black). e) Optical phonon dispersions for bulk GaSb and AlSb, calculated in DFT (dashed) and scaled to match literature values (solid), and confined phonon frequencies from Raman (green squares) and FIR-SE (circles).*

To start, we use an exemplary superlattice with thin (4ML) layers of GaSb and AlSb and with a large total superlattice thickness (~10 µm) to strongly reduce the contribution from the underlying substrate to the IR response. Within such a superlattice, the atomic displacement caused by confined phonons[62] can be described as:

$$u_m(B_2) \propto \cos\left(\frac{m\pi z}{n+\delta}\right),\ m = 1,3,5,\ldots \tag{2}$$

$$u_m(A_1) \propto \sin\left(\frac{m\pi z}{n+\delta}\right),\ m = 2,4,6,\ldots \tag{3}$$

The $m = 1$ mode (Fig. 2a) is typically much larger in amplitude than higher-order modes reported in prior Raman studies[40,46,48], indicating a larger oscillator strength, so we expect it to dominate the optical response. Using superlattice samples with spectrally distinct constituent Reststrahlen bands allows us to

confine the phonons within a single material, enabling individual control over the phonon properties in layered materials. This is differentiated from the previous reports of AlN/GaN atomic scale superlattices where the partially spectrally-overlapped Reststrahlen bands result in complex phonon interactions. These complex interactions necessitate fitting the optical response with a single uniaxial model of the dielectric function that masks how the phonons behave within the individual AlN or GaN layers. Here, our use of materials with spectrally-offset Reststrahlen bands eliminates folded optical phonon modes and allows us to extract the dielectric function of superlattice layers individually. This, in turn, allows for an assessment of the thickness dependence of the phonons within an individual, nanoscale-thickness material.

We measure Raman scattering from the surface of an 001-oriented superlattice under multiple polarization conditions with a 532-nm excitation laser, observing several features that vary with polarization (Fig. 2b). Under non-resonant conditions, cross-polarized Raman (z(xy)z, with the axes defined as x-[100], y-[010], z-[001]) preferentially scatters odd-ordered LO phonons, whereas parallel polarized Raman (z(xx)z) scatters more of the even-ordered LO phonons, as well as TO and interface phonons[63]. Using these rules, we can attribute the peaks in the parallel-polarized Raman spectra to the even-order confined phonons and interface modes, and the other prominent peaks in the cross-polarization spectra to odd-order confined LO modes (supplemental figure S4). The spectra show a strong LO_1 mode in both the GaSb and AlSb regions, as well as a much weaker LO_2 peak in the GaSb region. There are some weak background features that were previously attributed to large wavevector scattering processes and electronic transitions,[63] which we will not consider in this study.

To precisely determine the optical response of the thin layers of GaSb and AlSb, we leverage far-IR spectroscopic ellipsometry (FIR-SE) measurements of the 4ML/4ML superlattice (spectra in supplemental figure S5). Using the FIR-SE spectra, we model the dielectric function of each layer in the sample (GaSb substrate, 350-nm AlSb buffer, 3279 periods of 4ML AlSb/ 4ML GaSb, and a 5-nm GaSb capping layer) as a transverse-optical/longitudinal-optical (TOLO) oscillator. Bulk GaSb and AlSb are isotropic, and thick layers should be least affected by stress, so we treat the thick layers (substrate, buffer, capping layer) as isotropic. For the thin layers however, we expect the lightly strained unit cells to be uniaxial (see discussion in supplemental), so we model the 4ML layers as uniaxial TOLO oscillators. It is assumed in the modeling of the optical response that there is no variation between individual monolayers in the sample (i.e., one model for the 4ML GaSb, and another for the 4ML AlSb layers). The uniaxial TOLO model relies on the phonon frequencies, and a phonon damping term *γ*:

$$\varepsilon_j = \varepsilon_\infty \left(1 + \frac{\omega_{LO,j}^2 + \omega_{TO,j}^2}{\omega_{TO,j}^2 - \omega^2 - i\omega\gamma_j}\right) \qquad j = ex, ord \qquad (4)$$

Our ellipsometric model provides a dielectric function for the thick layers of GaSb and AlSb that are nominally bulk-like, lining up with literature values for bulk crystals, as well as our measurements of bulk samples, so we use these as the bulk dielectric functions for comparison.

We find the uniaxial TOLO model for the 4ML-thick layers, repeated for 3279 periods, provides an excellent fit to the FIR-SE measurements (parameters in supplemental table 1), suggesting that the optical response is indeed dominated by a single pair of TO and LO phonons in each of the ordinary and extraordinary functions, and for each of the bulk-like layers. However, the TOLO resonance is red-shifted and broadened along both axes (ordinary and extraordinary) compared to the bulk dielectric function, for both GaSb and AlSb (Fig. 2c,d). We expected the ordinary and extraordinary phonon frequencies to

diverge since the layer thickness is only confined in the ordinary axis. Instead, the phonon frequencies are only slightly offset, but the extraordinary TOLO resonance is further broadened compared to the ordinary axis – perhaps as a result of the small uniaxial strain in the superlattice. The magnitudes of the overall shifts, however, are much larger than we would expect for strain-induced effects in this system.

The altered dielectric function of the thin layers acquired from FIR-SE and the emergence of confined modes in the Raman response are indicative of confined phonon modes. However, in order for this change in the dielectric function to provide an effective design tool, the effects must be understood at a predictable level – building upon the phonon confinement models from the literature. To then investigate whether the phonon shifts are attributable to confinement effects, we use Eq. 1 to map the measured phonon frequencies from Raman and FIR-SE measurements to a calculated bulk phonon dispersion in the Γ-X Brillouin zone (superlattice direction) for GaSb and AlSb (Fig. 2e).

The calculated phonon dispersions from *ab initio* electronic structure theory calculations (faint dashed lines in Fig. 2e) rely on functionals which typically over-estimate lattice parameters[64], so they fall short of experimental phonon frequencies. To compensate for this discrepancy, we scale the dispersion curves to better match our measurements and literature values of the bulk phonon frequencies at the Γ-point (solid lines in Fig. 2e). For the measured LO phonons, we use a δ value of 1, indicating that the vibrational amplitude of the confined phonon terminates at the first anion atom (Al or Ga) after the interface (Fig. 2a). We find that for both the Raman measurements (black circles) and the phonon frequencies extracted from the FIR-SE measurements, the observed phonons correspond well to a confined *m*=1 mode. The ordinary and extraordinary phonon frequencies from our ellipsometric modeling both agree well with the confinement model shifts, with small offsets that correspond to the direction we would expect from strain (discussion in supplemental). The Raman peaks line up very closely to the extraordinary phonons from FIR-SE.

Using this same model indicates that the TO modes are not as confined as are the LO phonon modes. Specifically, unlike the LO phonons in which the mode dispersion could be matched with a δ = 1 value in Eq. 1, the confined TO modes required δ = 3 to obtain correspondence with the bulk dispersion for both those in AlSb and GaSb. The larger value of δ is indicative of a longer vibrational extent of the confined phonon across the interface, as shown in Fig. 2a, suggesting that the confined TO phonon vibration continues for one ML past the interface and stops at the next anion atom. The discrepancy in confinement between TO and LO modes is not without precedent. Within GaAs/AlAs superlattices, for example, a different degree of confinement was also reported for TO phonons (δ = 0) compared to LO phonons (δ = 1) using the same model[46,50,51].

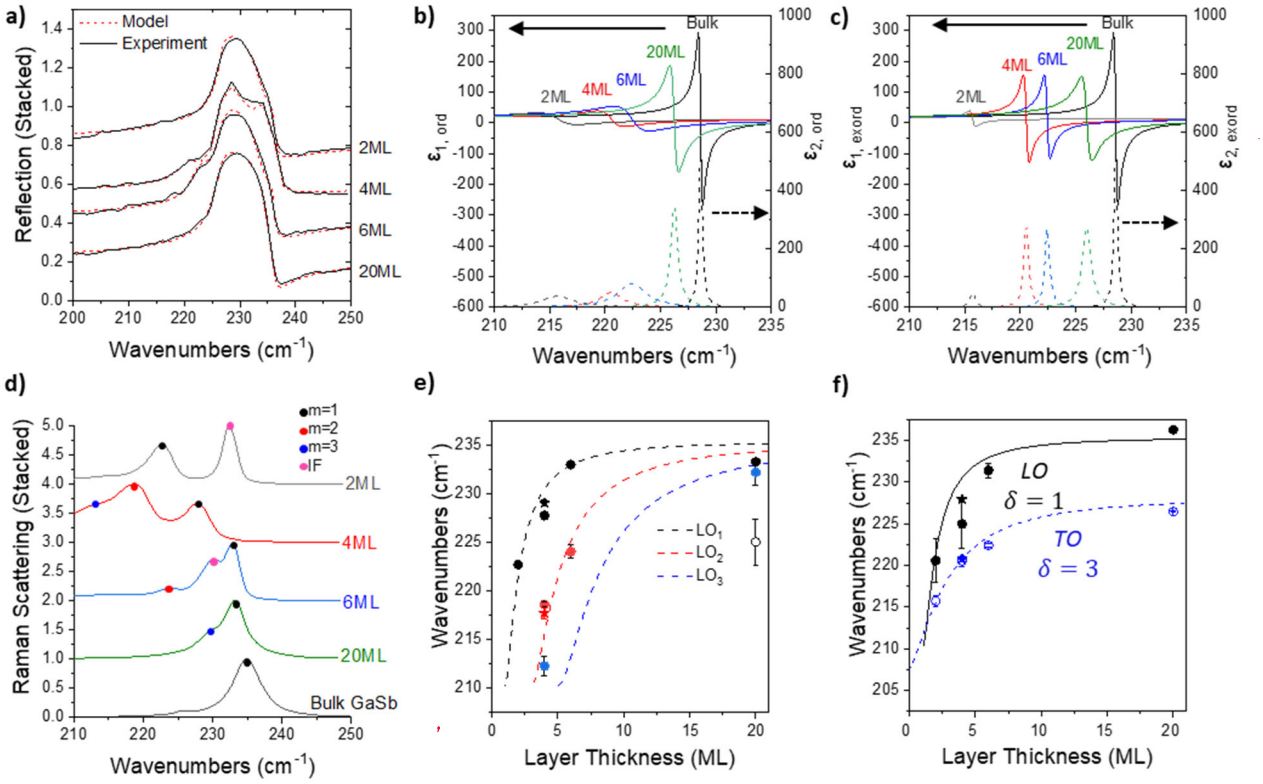

Figure 3: Exploring thickness dependence of phonon confinement. a) FTIR reflectance spectra of superlattices with 20ML AlSb alternating with varying thicknesses of GaSb. b) Ordinary dielectric function of GaSb layer at varying GaSb layer thicknesses, as extracted from FTIR studies. c) Extraordinary dielectric function of GaSb layer at varying thicknesses. d) Raman measurements of confined GaSb phonons for varying GaSb layer thicknesses. e) Confined phonon peaks from Raman (d), plotted against the confined phonon dispersion (dashed lines). Measurements of the 4ML/4ML superlattice from Fig. 2 included as stars. f) Ordinary phonon frequencies from (b), plotted against the confined phonon dispersion (m=1). Phonon frequencies from ellipsometry (Fig. 2) plotted as stars.

While the optical phonons observed in the 4ML/4ML superlattice appeared to show phonon confinement-induced changes to both the AlSb and GaSb phonons, we cannot make any conclusive observations from a single superlattice sample. In order to use the layer thickness to engineer the phonon properties, we must understand how phonon confinement develops as the layer thickness changes. The LO phonon dispersion along Γ-X is much less dispersive than the GaSb phonon dispersions, making it more difficult to discern confined LO phonons in the AlSb layers. Therefore, we focus on further exploration of the GaSb optical phonons.

To explore the impact of the changing layer-thickness, we use samples consisting of superlattices with 20ML-thick AlSb layers alternating with GaSb layers with thicknesses of 20, 6, 4, and 2ML. Here, 20ML was chosen for the AlSb layer as this was determined to be 'bulk-like', that is at this thickness the material could be well described using the bulk dielectric function. As such, by modifying the thickness of the GaSb while maintaining AlSb thickness, we can extract the role of phonon confinement upon the former, without any corresponding influences driven by the latter. Measuring the reflectance (at 55° incidence) using a Fourier Transform infrared (FTIR) spectrometer (Fig. 3a), we observe the underlying Reststrahlen band from the bulk GaSb substrate in tandem with subtler features arising from the superlattice layers

that shift with the change in layer-thickness. Using the same method of permittivity modelling as used with the previous FIR-SE data, we extract the dielectric function of the GaSb layers (Fig. 3b,c) as a function of thickness. With FTIR at such incident angles we are less sensitive to the extraordinary optical response, so we fix the extraordinary TO phonon frequency equal to the ordinary TO phonon frequency, which did not diverge strongly at 4ML (Fig. 2e). From the extracted dielectric function, we clearly see the phonon resonance redshift and broaden with decreasing thickness (Fig. 3b,c). The staggered trend in the extraordinary amplitude (Fig. 3c) is attributed to our decreased sensitivity, otherwise theres is a similar shift in the optical response along the ordinary and extraordinary axes.

We also characterize these thickness-varying superlattices with Raman spectroscopy (Fig. 3d). In these samples, we observe multiple peaks corresponding up to the $m = 3$ confined LO phonons that shift monotonically with the changing layer-thickness. We also observe strong peaks in a few samples that do not correspond to confined phonons. From the Raman selection rules discussed previously, we attribute these to interface phonons beyond the scope of the present study.

Confined phonons are typically measured, assigned a momentum via Eq. 1, and plotted on the bulk phonon dispersion as in Fig. 2e. However, while this method can support the identification of confined phonons, it prevents separation of different modal orders and layer thicknesses. Instead, if we consider Eq. 1 for a specific mode order *m*, and interface leakage δ, we have a constant ratio between the confined momentum and the layer thickness. Therefore, we can invert Eq. 1 to get an expression for the confined phonon dispersion for each order mode, which is a function of the number of MLs *n*.

$$\mathrm{k_0(m) = k(m) \div \frac{\pi}{d_0} = \frac{2m}{n+\delta}} \tag{5}$$

$$\mathrm{n = \frac{2m}{k_0} - \delta} \tag{6}$$

If we use this expression, we can map the bulk phonon dispersion (a function of momentum, *k*) to the confined thickness (a function of layer thickness in ML, *n*) to get the thickness-dispersion for the different order confined phonon modes (Fig. 3e,f). Note that for this we must choose a value for δ, which simply shifts the curve to the left or right on the x-axis. As in Fig. 2, we use δ=1 for the LO phonons, and δ=3 for the TO phonons. The relationship between the confined momentum and the layer thickness also provides some insight into the ideal thickness range for controlling the momentum (supplemental figure S7).

Using this confined phonon dispersion, we can overlay the observed Raman peaks for the different GaSb thicknesses and see how the confined phonons disperse as a function of the layer thickness (Fig. 3e). This confined phonon dispersion exaggerates any deviation from the confinement model but clearly demonstrates the thickness-dependent shift of the various-order phonons that results from phonon confinement and can be used to evaluate the engineering potential. Significant first-order phonon shifts occur in GaSb with thicknesses up to about 8ML, after which the frequency asymptotically approaches its bulk value (Fig. 3e). The confined phonons observed in Raman also match with the confined phonon dispersion, with the higher-order modes exhibiting larger shifts and a wider range of thickness tunability.

The TO and LO phonons extracted from FTIR measurements track well with the *m=1* confined phonon dispersion (Fig. 3f). The thickness dependent behavior of the TO phonons agrees very well with a δ value of 3 – supporting our observations from the 4ML/4ML superlattice in Figure 2. The extracted LO phonons follow the confined phonon dispersion well, but because LO phonons are not IR-active, and thus can only

be extracted via a fit to the reflection spectra, these measurements exhibit larger error bars. We also note here that the confined GaSb phonons measured in the 4ML/4ML superlattice agree well with those observed in a 4ML GaSb / 20ML AlSb superlattice (Fig. 3e-f stars indicate 4ML/4ML sample). This suggests that in spite of the interface leakage described by δ, phonon confinement is largely tolerant of the barrier layer width (i.e. GaSb phonon confinement is only a function of the GaSb layer thickness).

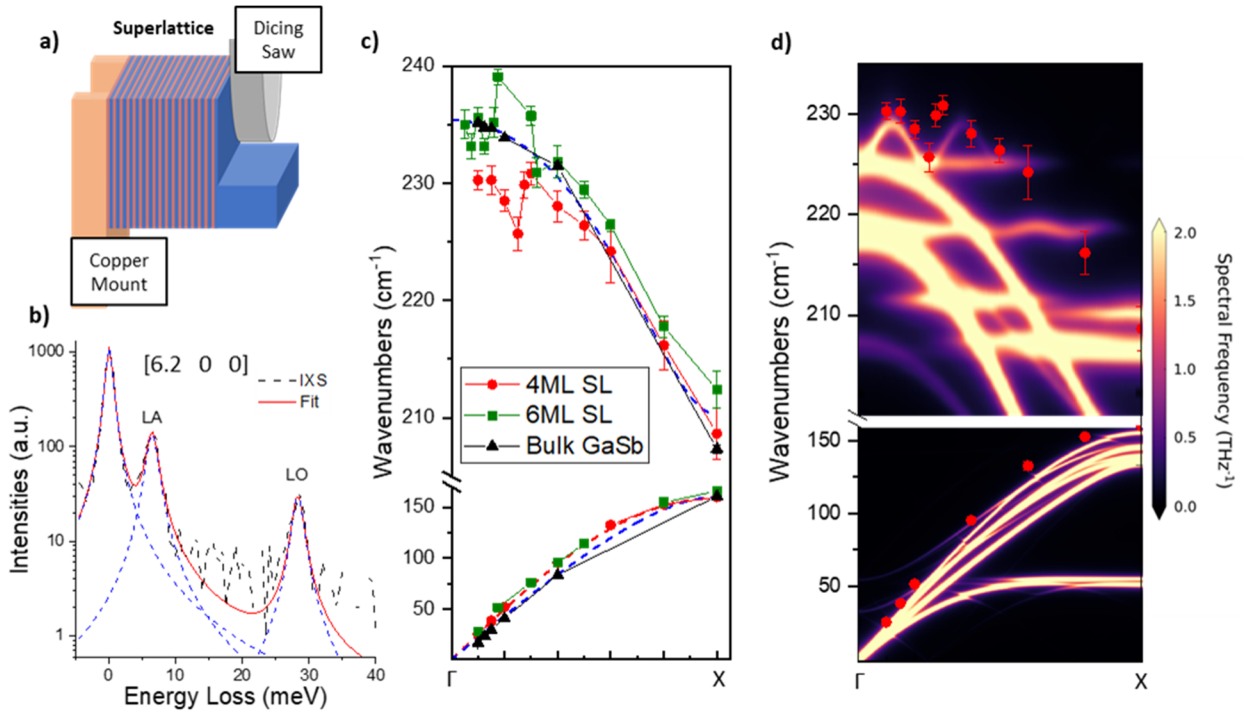

Figure 4: High-resolution momentum resolved inelastic X-ray scattering to probe the superlattice phonon dispersion. a) Schematic of mechanically thinning the substrate supporting the superlattice sample (The sample was not mounted on a cooper post during dicing, it was mounted on a copper post during the measurements). b) Inelastic X-ray scattering spectrum, with peak-fits showing the elastic (zero loss) peak, the longitudinal acoustic phonon peak, and longitudinal optical phonon peak, at 0.2 reduced momentum in the Γ-X Brillouin Zone. c) LO and LA phonon peaks observed in inelastic X-ray scattering of bulk GaSb (black triangles), the 4ML superlattice from Fig. 2 (red circles), and a 6ML GaSb/ 6ML AlSb superlattice (green squares) Overlaid on LO and LA dispersions of bulk GaSb (blue dashed lines) and bulk AlSb (red dashed lines). d) Calculated phonon density of states of 4ML GaSb/ 4ML AlSb superlattice, with overlaid IXS LO phonon peaks.

It has been conclusively shown that optical phonon confinement in thin films dramatically changes the optical phonon properties at the Γ-point. This becomes a useful tool, as we have shown here, for manipulating the infrared dielectric function of polar materials. Optical phonons also play a key role in many other applications involving phonon scattering processes. The ability to engineer the phonon dispersion could also become a valuable tool for engineering the phonon scattering properties. From the Γ-point measurements, it is clear that phonon confinement alters the phonon dispersion – but the size of superlattices is incompatible with metrologies such as neutron scattering, which typically requires bulk samples, precluding direct measurements of the confinement-induced changes to the full phonon dispersion across the Brillouin zone.

High-energy-resolution inelastic x-ray scattering[65] is an alternative to neutron scattering that allows for momentum and energy-resolved measurements of the phonons on smaller samples, down to a few microns in size. To that end, the 4ML/4ML superlattice discussed in Fig. 2 was grown to an overall superlattice thickness of ~10 μm. For comparison, we also grew a 6ML GaSb/ 6ML AlSb sample with similar overall thickness, the 4ML and 6ML samples were grown on GaSb substrate. The bulk GaSb substrate of these samples introduced additional phonon scattering due to the large penetration of the x-ray beam, (23.72 keV), which interfered with the signal coming from the superlattice. To minimize the scattering from the substrate and isolate the scattering signal to the superlattice, we thinned down most of the substrate supporting the 4ML superlattice using a diamond dicing machine, as demonstrated in Fig. 4a. As a result we were able to remove most of the substrate, so that the overall sample thickness was within a few μm of the superlattice thickness. The 4ML superlattice was then mounted on a copper holder on the HERIX spectrometer at sector 30 at the Advanced Photon Source, with the measurements performed in transmission mode. Following the substrate removal, we then measured the energy loss spectrum by scanning the energy of the incident x-ray beam at a fixed momentum. From our choice of momentum, we selectively scatter from the longitudinal phonons (Fig. 4b) and map out the Γ-X Brillouin zone (Fig. 4c). The measurements were performed close to the (600) Bragg peak.

Our measurements of a bulk GaSb substrate align very well with the longitudinal phonon dispersion we calculated using DFT (after shifting to match Raman frequencies), confirming our bulk GaSb phonon dispersion. The observed phonon features in the 4ML and 6ML superlattices also agree well in the acoustic phonon regime, albeit with a slight blue-shift resulting from the addition of AlSb acoustic phonons, which are too closely overlapped to resolve in IXS. At higher momenta near the X-point, the LO phonons of the superlattice also largely agree with the bulk GaSb phonons outside of some energy offset we attribute to strain induced by the mechanical thinning. However, near the confined layer thickness (~1/4 for the 4ML superlattice, and ~1/6 and ~1/3 for the 6ML superlattice) there is a marked deviation from the slowly dispersing bulk trends. To understand this deviation, we calculated the phonon dispersion for a 4ML GaSb / 4ML AlSb superlattice in DFT (Fig. 4d). As in figure 2e, these calculations rely on functionals which overestimate the lattice parameters (hence underestimating the phonon frequencies), and unfolding the superlattice phonons (in order to gain insight into the superlattice modes) prevents us from including an empirical TO-LO splitting offset to the LO branch, so the bulk-like mode is shifted down in frequency. We observe a new superlattice feature near the Γ-point that damps out quickly with increasing momentum. This feature appears to align well with the feature observed in IXS (Fig. 4d). The AlSb phonons are too weakly scattering and high energy to observe in IXS, but in the calculated DFT dispersion there is a similar superlattice feature to the one we see in the GaSb region (supplemental Fig. S6). The observed deviation from bulk phonon behavior suggests that in a thin-film, a low momentum (longer wavelength) optical phonon is significantly affected by the surrounding environment, reaching a peak when the phonon forms a standing wave within the film, and undergoes confinement (shifting the phonon frequency), while the higher momentum (short wavelength) phonons away from the Γ-point are largely unaffected by the layer thickness and behave as they would in a bulk crystal.

Our IXS measurements, coupled with *ab initio* calculations support the idea that phonon confinement impacts the off- Γ phonon dispersion. These results suggest that the phonon confinement effect results in a highly dispersive phonon branch that dominates the scattering behavior near the Γ-point, while the phonon behavior approaches the bulk dispersion as the momentum increases. This behavior is inherently different from zone-folding and other superlattice effects which have been demonstrated previously.

Conclusion

Here, we have shown that optical phonon confinement in thin film superlattices can be employed to directly modify the IR dielectric function of the material. We have also shown that this phonon confinement is primarily a function of the individual layer thickness rather than superlattice periodicity, offering the possibility to modify the constituent phonon behavior independently of the overall superlattice anisotropy. Additionally, we have provided an alternative view of the phonon confinement model, which enables predictions of optical phonon properties in thin films that may be useful for IR optics, but also for applications benefiting from controlling optical phonon behavior at the atomic scale, such as recent demonstrations of phonon polariton assisted thermal conduction[66,67]. We demonstrate some initial efforts to understand the impact of confinement on the phonon dispersion, which may have significant consequences in phonon scattering applications.

Methods

Sample Growth: The short period superlattices studied in this work were grown using a Veeco GENxplor molecular beam epitaxy (MBE) system. The primary superlattices consisted of 20 ML of AlSb, alternating with varying thickness (20,6,4,2) ML of GaSb, to a total thickness of roughly 1000nm. All samples were grown on (001)-oriented undoped GaSb substrates from Wafer Technology Ltd., with a 100nm GaSb buffer layer and a 5nm GaSb capping layer. The 4ML GaSb/4ML AlSb superlattice from Fig. 2 was grown to an 8um total thickness, with a 350nm AlSb buffer layer, and 5nm GaSb capping layer. Further details can be found here[61].

Raman Scattering: Raman spectroscopy was performed utilizing a WiTec alpha300R Raman system employing a 532 nm. All measurements performed in a backscattering arrangement with incident light p-polarized and focused with a 50X/0.55 NA objective. The collected Raman scattered light is dispersed using a 2400 l/mm grating resulting in accuracy of ~0.2 cm-1 and collected both with and without a polarization analyzer.

Phonon Dispersion Calculations: Phonon dispersions and eigenvectors were calculated, for bulk GaSb and AlSb as-well as the 4ML/4ML super-lattice, from first principles using the density functional theory formalism as implemented in the Vienna Ab initio Simulation Package (VASP)[68,69] and the frozen-phonon method as implemented in the PHONOPY package[70]. We use the VASP projector-augmented wave (PAW) pseudopotentials and converge the Hellmann-Feynman forces to 25 μeV/A using a plane-wave energy cutoff of 600 eV and a (12x12x12) 12x12x1 Γ-centered k-point mesh to sample the Brillouin zone of the (bulk) super-lattice geometry respectively. For the exchange-correlation functional, we choose the Perdew-Burke-Ernzerhof revised for solids (PBEsol) form of the generalized gradient approximation (GGA)[71]. After computing the force constants on the 4ML/4ML superlattice, an effective phonon band structure is unfolded onto the bulk unit-cell using the projection operators of the small representation of the little groups as implemented in the upho package[72].

Far Infrared Spectroscopic Ellipsometry: Far-infrared ellipsometry was performed from 100 cm^{-1}–500 cm^{-1} using an in-house built FIR-VASE ellipsometer[73]. Data were acquired in Mueller matrix format as well as in isotropic Psi-Delta format at angles of incidence of Φ_a = 50°, 60°, and and 70°. Measurements were performed with a resolution on 1m^{-1} in stable, ambient conditions at room temperature.

Fourier-Transform Infrared Spectroscopy: Mid- to far-infrared, angle-resolved reflectance measurements were taken using a Pike Technologies VeeMax variable angle specular reflectance accessory coupled to a Bruker Vertex 70v FTIR spectrometer, equipped with a broadband DTGS detector, and a wide range FIR beam-splitter (30-6000 cm^{-1}). A polyethylene wire grid polarizer was used to collect s- and p-polarized light.

Dielectric Fitting: Dielectric function extraction was performed using the WVASE software (J.A. Woolam). The superlattice dielectric functions were fit on a layer-by-layer basis, by linking the dielectric functions of matched layers.

Inelastic X-ray Scattering

Acknowledgements:

J.M. and G.V. acknowledge funding from the National Science Foundation under grant NSF-DMR-1904793., while J.D.C. was supported by the Office of Naval Research grant #N00014-22-1-2035. M.S. acknowledges support by the National Science Foundation (**NSF) under awards DMR 1808715 and OIA-2044049, by** Air Force Office of **Scientific Research under awards FA9550-18-1-0360, FA9550-19-S-0003, and FA9550-21-1-0259, by the Knut and Alice Wallenbergs Foundation award 'Wide-bandgap semiconductors for next generation quantum components', and by the J.A.Woollam Foundation. M. N. A., P. S. and S. L. acknowledge funding from the National Science Foundation, Division of Materials Research under Award No. 1904760.** M.N.A., P. S., and S.L. acknowledge the use of the Materials Growth Facility (MGF) at the University of Delaware, which is partially supported by the National Science Foundation Major Research Instrumentation under Grant No. 1828141 and UD-CHARM a National Science Foundation MRSEC under Award No. DMR-2011824.This research used resources of the Oak Ridge Leadership Computing Facility, which is a DOE Office of Science User Facility supported under Contract DE-AC05-00OR22725 as well as the resources of the National Energy Research Scientific Computing Center, a DOE Office of Science User Facility supported by the Office of Science of the U.S. Department of Energy under Contract No. DE-AC02-05CH11231. P.N. is a Moore Inventor Fellow and gratefully acknowledges support through Grant No. GBMF8048 from the Gordon and Betty Moore Foundation.

This research used resources of the Advanced Photon Source, a U.S. Department of Energy (DOE) Office of Science user facility operated for the DOE Office of Science by Argonne National Laboratory under Contract No. DE-AC02-06CH11357.

References

1. Folland, T. G., Nordin, L., Wasserman, D. & Caldwell, J. D. Probing polaritons in the mid- to far-infrared. *J. Appl. Phys.* **125**, 191102 (2019).

2. Basov, D. N., Fogler, M. M. & García De Abajo, F. J. Polaritons in van der Waals materials. *Science (80-.).* **354**, (2016).

3. Low, T. *et al.* Polaritons in layered two-dimensional materials. *Nat. Mater.* **16**, 182–194 (2016).

4. Caldwell, J. D. *et al.* Low-loss, infrared and terahertz nanophotonics using surface phonon polaritons. *Nanophotonics* vol. 4 44–68 (2015).

5. Foteinopoulou, S., Devarapu, G. C. R., Subramania, G. S., Krishna, S. & Wasserman, D. Phonon-polaritonics: Enabling powerful capabilities for infrared photonics. *Nanophotonics* **8**, 2129–2175 (2019).

6. Adachi, S. *The Reststrahlen Region*. *Optical Properties of Crystalline and Amorphous Semiconductors* (Springer, Boston, MA, 1999). doi:10.1007/978-1-4615-5241-3_2.

7. Hofmann, T., Leibiger, G., Gottschalch, V., Pietzonka, I. & Schubert, M. Infrared dielectric function and phonon modes of highly disordered (Al x Ga 1 − x) 0.52 In 0.48 P. *Phys. Rev. B* **64**, 155206 (2001).

8. Stokey, M. *et al.* Infrared-active phonon modes and static dielectric constants in α-(AlxGa1−x)2O3 ($0.18 \leq x \leq 0.54$) alloys. *Appl. Phys. Lett.* **120**, 112202 (2022).

9. Taboada-Gutiérrez, J. *et al.* Broad spectral tuning of ultra-low-loss polaritons in a van der Waals crystal by intercalation. *Nat. Mater.* **19**, 964–968 (2020).

10. Giles, A. J. *et al.* Ultralow-loss polaritons in isotopically pure boron nitride. *Nat. Mater.* **17**, (2018).

11. Cuscó, R. *et al.* Isotopic effects on phonon anharmonicity in layered van der Waals crystals: Isotopically pure hexagonal boron nitride. *Phys. Rev. B* **97**, (2018).

12. He, M. *et al.* Phonon engineering of boron nitride via isotopic enrichment. *J. Mater. Res.* **36**, 4394–4403 (2021).

13. Spann, B. T. *et al.* Photoinduced tunability of the reststrahlen band in 4H-SiC. *Phys. Rev. B* **93**, 085205 (2016).

14. Adam D. Dunkelberger, Chase T. Ellis, Daniel C. Ratchford, Alexander J. Giles, Mijin Kim, Chul Soo Kim, Bryan T. Spann, Igor Vurgaftman, Joseph G. Tischler, James P. Long, Orest J. Glembocki, J. C. O. & J. D. C. Active tuning of surface phonon polariton resonances via carrier photoinjection. *Nat. Photonics* **12**, 50–56 (2018).

15. Bensmann, S. *et al.* Near-field imaging and spectroscopy of locally strained GaN using an IR broadband laser. *Opt. Express* **22**, 22369 (2014).

16. Huber, A. J., Wittborn, J. & Hillenbrand, R. Infrared spectroscopic near-field mapping of single nanotransistors. *Nanotechnology* **21**, (2010).

17. Korlacki, R. *et al.* Strain and stress relationships for optical phonon modes in monoclinic crystals

with +¦-Ga2 O3 as an example. *Phys. Rev. B* **102**, (2020).

18. Tekippe, V. J., Ramdas, A. K. & Rodriguez, S. Piezospectroscopic study of the Raman spectrum of α-quartz. *Phys. Rev. B* **8**, 706–717 (1973).

19. Briggs, R. J. & Ramdas, A. K. Piezospectroscopic study of the raman spectrum of cadmium sulfide. *Phys. Rev. B* **13**, 5518–5529 (1976).

20. Bir, G. L. & Pikus, G. E. *Symmetry and strain-induced effects in semiconductors*. *Materials Research* (John Wiley & Sons, 1974).

21. Dai, S. *et al.* Subdiffractional focusing and guiding of polaritonic rays in a natural hyperbolic material. *Nat. Commun.* **6**, (2015).

22. Caldwell, J. D. *et al.* Sub-diffractional volume-confined polaritons in the natural hyperbolic material hexagonal boron nitride. *Nat. Commun.* **5**, (2014).

23. Poddubny, A., Iorsh, I., Belov, P. & Kivshar, Y. Hyperbolic metamaterials. *Nat. Photonics* **7**, 948–957 (2013).

24. Li, P. *et al.* Hyperbolic phonon-polaritons in boron nitride for near-field optical imaging and focusing. *Nat. Commun.* **6**, 7507 (2015).

25. Li, P. *et al.* Hyperbolic phonon-polaritons in boron nitride for near-field optical imaging and focusing. *Nat. Commun.* **6**, 1–9 (2015).

26. Caldwell, J. D. *et al.* Photonics with hexagonal boron nitride. *Nat. Rev. Mater.* **4**, 552–567 (2019).

27. Ma, W. *et al.* In-plane anisotropic and ultra-low-loss polaritons in a natural van der Waals crystal. *Nature* **562**, 557–562 (2018).

28. Zheng, Z. *et al.* Highly Confined and Tunable Hyperbolic Phonon Polaritons in Van Der Waals Semiconducting Transition Metal Oxides. *Adv. Mater.* **30**, 1705318 (2018).

29. Dai, Z. *et al.* Edge-oriented and steerable hyperbolic polaritons in anisotropic van der Waals nanocavities. *Nat. Commun.* **11**, 1–8 (2020).

30. Duan, J. *et al.* Twisted Nano-Optics: Manipulating Light at the Nanoscale with Twisted Phonon Polaritonic Slabs. *Nano Lett.* **20**, 5323–5329 (2020).

31. Hu, G. *et al.* Topological polaritons and photonic magic angles in twisted α-MoO3 bilayers. *Nature* **582**, 209–213 (2020).

32. Chen, M. *et al.* Configurable phonon polaritons in twisted α-MoO3. *Nat. Mater.* **19**, 1307–1311 (2020).

33. Álvarez-Pérez, G. *et al.* Infrared Permittivity of the Biaxial van der Waals Semiconductor α-MoO3 from Near- and Far-Field Correlative Studies. *Adv. Mater.* **32**, (2020).

34. Passler, N. C. *et al.* Hyperbolic shear polaritons in low-symmetry crystals. *Nature* **602**, 595–600 (2022).

35. Zheng, Z. *et al.* Phonon Polaritons in Twisted Double-Layers of Hyperbolic van der Waals Crystals. *Nano Lett.* **20**, 5301–5308 (2020).

36. He, M. *et al.* Anisotropy and Modal Hybridization in Infrared Nanophotonics Using Low-Symmetry Materials. *ACS Photonics* (2021) doi:10.1021/ACSPHOTONICS.1C01486/ASSET/IMAGES/MEDIUM/PH1C01486_0011.GIF.

37. Álvarez-Pérez, G. *et al.* Active Tuning of Highly Anisotropic Phonon Polaritons in Van der Waals Crystal Slabs by Gated Graphene. *ACS Photonics* **9**, 383–390 (2022).

38. Ratchford, D. C. *et al.* Controlling the Infrared Dielectric Function through Atomic-Scale Heterostructures. *ACS Nano* **13**, (2019).

39. Caldwell, J. D. & Novoselov, K. S. Mid-infrared nanophotonics. *Nat. Mater.* **14**, 364–366 (2015).

40. Nakayama, M. *et al.* Zone-folding effects on phonons in gaas-alas superlattices. *Jpn. J. Appl. Phys.* **24**, 1331–1334 (1985).

41. Barker, A. S., Merz, J. L. & Gossard, A. C. Study of zone-folding effects on phonons in alternating monolayers of GaAs-AlAs. *Phys. Rev. B* **17**, 3181–3196 (1978).

42. Dechaumphai, E. & Chen, R. Thermal transport in phononic crystals: The role of zone folding effect. *J. Appl. Phys.* **111**, 073508 (2012).

43. Hopkins, P. E. *et al.* Reduction in the thermal conductivity of single crystalline silicon by phononic crystal patterning. *Nano Lett.* **11**, 107–112 (2011).

44. Nakashima, S. & Harima, H. Raman Investigation of SiC Polytypes. *Phys. status solidi* **162**, 39–64 (1997).

45. Gubbin, C. R. *et al.* Hybrid longitudinal-transverse phonon polaritons. *Nat. Commun.* **10**, 1–6 (2019).

46. Sood, A. K., Menéndez, J., Cardona, M. & Ploog, K. Resonance Raman scattering by confined LO and TO phonons in GaAs-AlAs superlattices. *Phys. Rev. Lett.* **54**, 2111–2114 (1985).

47. Molinari, E., Fasolino, A. & Kunc, K. Confined longitudinal and transverse phonons in GaAs/AlAs superlattices. *Superlattices Microstruct.* **2**, 397–400 (1986).

48. Molinari, E., Fasolino, A. & Kunc, K. Superlattice effects on confined phonons. *Phys. Rev. Lett.* **56**, 1751 (1986).

49. Da Silva, S. W. *et al.* Optical phonon spectra of GaSb/AlSb superlattices: Influence of strain and interface roughnesses. *J. Appl. Phys.* **80**, 597–599 (1996).

50. Jusserand, B. & Paquet, D. Comment on 'resonance raman scattering by confined LO and to phonons in gaAs-alAs superlattices'. *Phys. Rev. Lett.* **56**, 1752 (1986).

51. Sood, A. K., Menéndez, J., Cardona, M. & Ploog, K. Sood et al. respond. *Phys. Rev. Lett.* **56**, 1753 (1986).

52. Hoglund, E. R. *et al.* Emergent interface vibrational structure of oxide superlattices. *Nature* **601**, 556–561 (2022).

53. Armelles, G., Recio, M., Ruiz, A. & Briones, F. Confined optical phonons in GaAs/GaP strained layer superlattices. *Solid State Commun.* **71**, 431–434 (1989).

54. D. Berdekas, G. K. Phonon confinement in InAs/GaSb superlattices. **43**, 9976–9979 (1991).

55. Katayama, S. I. & Fukasawa, R. Raman Spectra of Confined LO Phonons in Single Heterostructure. *J. Phys. Soc. Japan* **56**, 3726–3733 (1987).

56. Momma, K. & Izumi, F. VESTA 3 for three-dimensional visualization of crystal, volumetric and morphology data. *urn:issn:0021-8898* **44**, 1272–1276 (2011).

57. Darakchieva, V. *et al.* Phonon mode behavior in strained wurtzite AlN/GaN superlattices. *Phys. Rev. B - Condens. Matter Mater. Phys.* **71**, 115329 (2005).

58. Kroemer, H. The 6.1Å family (InAs, GaSb, AlSb) and its heterostructures: a selective review. *Phys. E Low-dimensional Syst. Nanostructures* **20**, 196–203 (2004).

59. Dutta, P. S., Bhat, H. L. & Kumar, V. The physics and technology of gallium antimonide: An emerging optoelectronic material. *J. Appl. Phys.* **81**, 5821–5870 (1997).

60. Bennett, B. R., Magno, R., Boos, J. B., Kruppa, W. & Ancona, M. G. Antimonide-based compound semiconductors for electronic devices: A review. *Solid. State. Electron.* **49**, 1875–1895 (2005).

61. Alam, M. N., Matson, J. R., Sohr, P., Caldwell, J. D. & Law, S. Interface quality in GaSb/AlSb short period superlattices. (2021) doi:10.1116/6.0001290.

62. Richter, E. & Strauch, D. Lattice dynamics of GaAs/AlAs superlattices. *Solid State Commun.* **64**, 867–870 (1987).

63. Schwartz, G. P., Gualtieri, G. J., Sunder, W. A. & Farrow, L. A. Light scattering from quantum confined and interface optical vibrational modes in strained-layer GaSb/AlSb superlattices. *Phys. Rev. B* **36**, 4868–4877 (1987).

64. Yip, S. *et al.* Physical Properties of III-Antiminodes-a First Principles Study You may also like Recent advances in III-Sb nanowires: from synthesis to applications Demonstration of Sn-seeded GaSb homo-and GaAs-GaSb heterostructural nanowires Physical Properties of III-Antiminodes-a First Principles Study. *Commun. Theor. Phys. Commun. Theor. Phys* **52**, 527–533 (2009).

65. Said, A. H. *et al.* High-energy-resolution inelastic X-ray scattering spectrometer at beamline 30-ID of the Advanced Photon Source. *J. Synchrotron Radiat.* **27**, 827–835 (2020).

66. Hutchins, W. *et al.* Ultrafast evanescent heat transfer across solid state interfaces via phonon-polaritons. *Under Rev.* (2023).

67. Pan, Z. *et al.* Direct experimental evidence for phonon polariton mediated heat conduction. *Under Rev.* (2023).

68. Kresse, G. & Furthmüller, J. Efficiency of ab-initio total energy calculations for metals and semiconductors using a plane-wave basis set. *Comput. Mater. Sci.* **6**, 15–50 (1996).

69. Kresse, G. & Furthmüller, J. Efficient iterative schemes for ab initio total-energy calculations using a plane-wave basis set. *Phys. Rev. B - Condens. Matter Mater. Phys.* **54**, 11169–11186 (1996).

70. Togo, A. & Tanaka, I. First principles phonon calculations in materials science. *Scr. Mater.* **108**, 1–5 (2015).

71. Csonka, G. I. *et al.* Assessing the performance of recent density functionals for bulk solids. *Phys. Rev. B - Condens. Matter Mater. Phys.* **79**, (2009).

72. Ikeda, Y., Carreras, A., Seko, A., Togo, A. & Tanaka, I. Mode decomposition based on

crystallographic symmetry in the band-unfolding method. *Phys. Rev. B* **95**, (2017).

73. Kühne, P., Herzinger, C. M., Schubert, M., Woollam, J. A. & Hofmann, T. Invited Article: An integrated mid-infrared, far-infrared, and terahertz optical Hall effect instrument. *Rev. Sci. Instrum.* **85**, 071301 (2014).